Experimental Thermal and Fluid Science 149 (2023) 110995

Contents lists available at ScienceDirect

Experimental Thermal and Fluid Science

journal homepage: www.elsevier.com/locate/etfs

Characteristics of a tip-vortex generated by a single rotor used in agricultural spraying drone

Mehrzad Ansaripour [a], Reza Alidoost Dafsari [a], Seung-Hwa Yu [b], Yong Choi [b], Jeekeun Lee [c,*]

[a] Department of Mechanical System Engineering, Graduate School, Jeonbuk National University, Republic of Korea
[b] National Institute of Agricultural Science, RDA, Republic of Korea
[c] Division of mechanical system Engineering, Jeonbuk National University, Republic of Korea

ARTICLE INFO

Keywords:
Tip vortex dynamics
Downwash flow
Rotor blade
Agricultural drone
Particle image velocimetry (PIV)

ABSTRACT

A better understanding of downwash flow is required to increase the efficiency of unmanned aerial vehicle sprayers. The tip vortex rolled up by the rotor blade tip rotating at high speed produces a complex induced velocity field, which has an important impact on the downwash flow in the wake of the rotor. Usually, a symmetrical experimental setup with a central rotor support perpendicular to the rotation plane is used in studies on rotating blade wake and vortices, potentially leading to differences in observed wake and vortices in real situations. whereas in reality, the rotor is typically supported by a parallel arm extending below the rotor in the rotation plane. It is crucial to consider these differences for accurate results in analyzing blade rotation. The behavior of the tip vortices, dynamic characteristics, and velocity field of the rotor wake in agricultural drone single-rotor downwash flow was experimentally investigated using particle image velocimetry (PIV) combined with high-speed camera imaging. The dynamics of blade tip vortices at different wake ages and rotational speeds of the rotor, 1000–3000 rpm, were measured and analyzed. The results indicate that in the early stages of a vortex's life, tip vortices generated by rotors do not have an axisymmetric structure, and the swirl velocity in the core decreases logarithmically as the wake age increases. Vortex models were validated by examining the swirl velocity structure of the tip of the vortex. Vortices within the vortex core exhibit a comparable self-similar velocity profile to the Iverson model's laminar profile, despite the transition flow outside the vortex core. With these measurements, the behavior of vortices in the rotor's wake could be described with generalized semi-empirical models.

1. Introduction

In recent years, agricultural UAVs have been increasingly used for pesticide spraying due to advances in unmanned aerial vehicle (UAV) technology [1,2]. With their ability to hover, maneuver, and take off and land vertically, rotary-wing UAVs provide significant advantages over fixed-wing drones [3]. Airborne sprayers have several benefits over conventional land-based apparatuses, including noncrop destruction operations, the treatment of large areas in a short amount of time, targeted spraying, and reduced inputs and operating costs [4,5]. Despite the targeted spraying advantage of UAVs, the turbulent downwash flow of the rotors can disrupt the spray structure and affect the disintegration of droplets [6,7]. In addition, it is not easy to fully understand spray drift associated with UAV applications, especially for fine droplets generated by spray nozzles, which has raised concerns for environmental and human safety [5,8].

The three-dimensional and unsteady flow in the wake of the rotor blade has been an exciting matter for researchers due to the correlation between the rotor's aerodynamics performance and wake structure and behavior [9]. Early studies indicated that the downwash flow in the wake region, where the spray nozzles are located is highly dynamic and complex due to the tip vortices and shear layer trailing from the blades [9,10]. While many studies have been conducted on tip-vortex formation, measurement, and characterization, the effect of the rotor blade tip vortex on the downwash flow and spray drift characteristics is not entirely understood. As far as the author knows, very few studies have been conducted on how rotating blades interact with spray on agricultural UAVs. Recent advances in agricultural unmanned aerial vehicles (UAVs) have made them increasingly popular for crop monitoring and spraying operations. While there is a growing body of research on the use of UAVs for agriculture-related applications, there is surprisingly

* Corresponding author.
E-mail address: leejk@jbnu.ac.kr (J. Lee).

https://doi.org/10.1016/j.expthermflusci.2023.110995
Received 20 March 2023; Received in revised form 18 May 2023; Accepted 30 June 2023
Available online 15 July 2023

Nomenclature

$A = 0.78$	Coefficient for Landgrebe equation
C_T	Rotor thrust coefficient, $C_T = Thrust/\rho\pi R^2(\Omega R)^2$
M	Number of points in the domain S of Γ_2 function
N_b	Number of blades
R_{tip}	Radius of blade (m)
S	Domain for evaluating Γ_2 function
V_{Btip}	Blade tip velocity (m/s)
V_θ	Vortex swirl velocity (m/s)
$V_{\theta max}$	Vortex maximum swirl velocity (m/s)
X_{tip}	Non-dimensional radial coordinate of tip vortex
Z_{tip}	Non-dimensional axial coordinate of tip vortex
c	Blade chord length
k_1, k_2	Coefficients for Landgrebe equation
$n = 2$	Vatistas model parameter
$\vec{r}$	Cartesian position vector
r_c	Vortex core radius (m)
u	Velocity component in radial direction (m/s)
v	Velocity component in axial direction (m/s)
x_i	Coordinates of point inside domain S (m)
x_j	Coordinates of point inside domain S (m)
Γ_2	Vortex detection function
$\Lambda = 0.145 + 27C_T$	Coefficient for Landgrebe equation
$\beta = 1.38$	Vatistas model parameter
σ	Rotor solidity, σ=blade area/rotor area
θ_{tw}	Blade linear twist, normally negative (deg)
ψ_w	Wake azimuth angle relative to the blade (deg)

little information on how the spray interacts with the downwash flow generated by the UAVs' rotors [11–13]. This lack of understanding is of particular importance for UAVs used for spraying operations. The downwash flow generated by the UAV's rotors affects the spray pattern, which in turn affects the amount of pesticide or fertilizer applied to the crops. In addition, the downwash flow can cause the spray droplets to drift away from the target area, leading to inefficient use of the pesticide or fertilizer. To better understand the interaction between the spray and the UAVs' downwash flow, further research is needed.

In recent years, many studies have been performed on vortex formation and behavior near the blade at early wake ages. The vortices were observed as void regions in early flow visualization measurements, which allowed for estimating the size of vortex cores and diffusion properties [14]. Not only could the downwash velocity field influence the droplet distribution, but the deposition zone of pesticides was also affected by the velocity field. The uniformity of droplet deposition would be increased with an increase in downwash velocity. In addition to the nozzle's location in the downwash flow, parameters such as droplet properties and nozzle-target positions influence droplet distribution [15].

Several studies have been conducted on vortex measurements and the near-wake behavior of vortices. Martin et al. [16] evaluated a high-resolution 3D velocity component measurement of trailing vortices in the wake of a hovering rotor regarding vortex formation, core structure, and vortex evolution up to 180°. Wake aging starts with a tip vortex core with a radius below 3% of the blade chord, but as it advances, the radius increases asymptotically.

Furthermore, vortex cores exhibit substantial axial velocity deficits at initial wake ages, but the deficits decrease rapidly as the vortex ages. Tip vortices, based on previous studies, exhibit neither laminar nor turbulent structures; instead, the structure continuously evolves. Understanding the various characteristics of rotor blade tip vortices is crucial for forecasting helicopter rotor performance and the resulting acoustics because, unlike fixed wings, which trail tip vortices downstream, rotor tip vortices hang around the blades and themselves for extended periods of time. Hence, multiple studies have tried to develop a mathematical model for tip vortex behavior prediction, including the velocity of tip vortices and vortex growth. Aside from predicting wake and tip vortex characteristics accurately, it appears that tip vortices have a significant impact on rotor performance [9,17,18].

The shape of blade tips is one factor that influences vortex characteristics [19,20]. Martin et al. [16 investigated the vortex characteristics of different blade tip shapes (rectangular, tapered, swept, and subwing tip). The ratio of peak swirl velocity to the axial velocity deficit is found to be a source of vortex core instability. There was a significant reduction in the initial peak swirl velocity because of the blade taper. Milluzzo et al. [21] experimentally studied wake behavior from a single rotor with different blade shapes in the presence of a horizontal ground plate. It was found that the blade shape has a significant role in developing the characteristics of the formed tip-vortex, especially during the roll-up process.

Numerical modeling of UAV wakes has been gaining interest in recent years. A numerical study of downwash flow inside canopies showed that the downwash flow was highly affected by load, canopy density and height, and operation height. The velocity inside a canopy directly correlates with the load and canopy diameters [22]. The simulation of the airflow field of study of the aerodynamic performance of amphibious UAVs for various flight conditions revealed that the wind speed and angle of attack have a significant impact on the performance and stability of the UAVs [23]. The airflow field of a UAV was evaluated in indoor conditions, and the results indicate that the airflow was highly affected by the indoor environment structure, and the UAV must fly at a higher height to achieve a spread airflow pattern [24]. The UAV's airflow field significantly influences spray droplet deposition and drift. The CFD simulation of a six-rotor agricultural UAV under different conditions shows that, as the flight condition differs from the optimal point, the size of eddies inside the wake increases and affects the droplet distribution and movement [25].

The formation and development of the tip vortex in the wake flow have a significant effect on vortex dynamics. Several studies utilized particle image velocimetry (PIV) to understand vortex development on the first revolution of the rotor [14]. There was an asymmetric swirl and axis velocity distribution relative to the vortex center. Approximately 53% of the maximum circulation remains within the vortex core during the first revolution [26]. Ramasamy et al. [27] evaluated turbulent vortex flow properties with stereoscopic digital particle image velocimetry (DPIV) measurements. They found that at all wake ages, the tip vortex was non-axisymmetric. An isotropic distribution of eddy viscosity was found in the measured turbulence characteristics. The hovering efficiency of micro rotating-wing air vehicles was low due to drag losses on the blades. The micro-UAV rotor wake flow field was thus experimentally measured at low chord Reynolds numbers [28]. The blade tip vortices did not reach total circulation until some distance downstream of the blade due to viscous effects, which are more significant at low Reynolds numbers. Initially, the blade tip vortices may not reach full circulation until some distance downstream from the blade after formation and roll-up due to viscous effects, which are more important at lower Reynolds numbers. As a result of the turbulent diffusion of vorticity following roll-up, the tip vortex core size increases.

To evaluate the vortex formation on the blade, Duraisamy et al. [29] studied the formation of helicopter blade tip vortices in hovering mode. Compressible Navier-Stokes equations were used to evaluate the flow in the discretized computation domain. The flow was measured using stereoscopic particle image velocimetry. The numerical results and

measured values reveal that multiple coherent structures characterize the vortex flow field at the tip of the rotor. Near the blade tip, crossflow separations produce secondary and tertiary vortices. Eventually, these vortices and the trailing wake sheets are entrained into the tip vortex. Johnson et al. [30] studied the formation and characteristics of a turbulent tip-vortex using dual-plane stereoscopic PIV. The findings show that stress and strain should not be modeled as linear functions of strain in blade tip vortices under an isotropic assumption of turbulence.

In addition to the interactions between the vortex and the downwash flow, the behavior of the tip vortex, as well as its formation and characteristics, are complex phenomena. Regarding this matter, several studies have been conducted. Milluzzo and Leishman [31] investigated the helicoidal vortex sheet using PIV measurements. Within rotor wakes, the interaction between sheets and tip vortices was observed, which depended on rotor thrust as well as blade twist. Both blade twist and rotor thrust influenced the tip vortices' radial positions. However, the axial locations exhibited smaller variations correlated to axial convection velocity differences. Shukla and Komerath [32] experimentally studied the interaction of two side-by-side rotors at different Reynolds numbers and rotor distances. Thrust and torque measurements show that rotor efficiency drops at small rotor spacings at low Reynolds numbers. For close-proximity rotors, a high inter-rotor wake interaction was observed.

Sutkowy et al. [33] studied the characteristics of a rotor wake at low Reynolds number. The aerodynamic inefficiency of rotors operating under a low Reynolds number condition, has been linked to specific features of the wake structure. Du et al. [34] studied tip-vortex identification and characteristics in the hovering state for two different collective pitches. Once again, it is confirmed that the blade shape significantly impacts the vortex characteristics and motion. Increasing the rotor's collective pitch increases the wake's radial contraction and axial displacement, as well as the blade tip vortex intensity.

Gregorio et al. [35] researched the characterization of a small-scale rotor wake numerically and experimentally in hovering conditions. A numerical simulation was conducted to evaluate the accuracy and modeling capabilities of the free-wake boundary element methodology. Despite reasonable agreement between the experimental and numerical estimates, the Blade Element Method simulations underestimated the diffusion effects. Compared to the experimental results, the shear layer regions were smaller. Wolf et al. [36] confirmed the presence of secondary vortices, which were first found in some computational studies [19,37,38]. Both Lagrangian tracks of flow and derived vortex identification criteria provided evidence of secondary vortex structures. The S-shaped secondary structure entangles the primary tip vortices. Schwarz et al. [39], by using a combination of stereoscopic particle image velocimetry measurements with high-fidelity simulations in different measurement planes, investigated secondary vortex structures in the wake of a two-bladed rotor in hover conditions. At various axial locations, secondary vortex structures were detected and quantified. At 0.8R below the rotor, the number of secondary vortices peaks. Simulations accurately captured secondary vortex structures, whereas experiments revealed weaker vortices.

Although there have been numerous studies on vortex dynamics and characteristics, the interaction between the tip vortex, the vortex sheet, and the downwash flow and how these three elements interact with each other remain to be fully understood. Developing a better understanding of wake flow behavior will allow us to reduce the spray droplet's drift potential and improve pesticide coverage ratios.

In most studies of the wake and vortices of rotating blades, researchers attempt to create an experimental setup that is as symmetrical as possible and provides support for the rotor at the center of the hub, perpendicular to the rotation plane. However, the rotor is usually supported by an arm extending below the rotor, parallel to the rotation plane of the blade. This arrangement of support differs significantly from the experimental configuration in previous studies, and as a result, the resulting wake and vortices may not be the same as those observed in real situations. It is therefore important to consider the differences between the actual support position and the experimental setup when analyzing the wake and vortices of rotating blades in order to ensure the most accurate results. The objective of the present study was to gain more understanding and knowledge regarding the tip vortex characteristics and dynamics in the wake of the two-blade rotor of a typical agricultural drone at different rotational speeds and wake ages in hovering conditions. Therefore, the flow field in the rotor's wake was studied using particle image velocimetry combined with a high-speed camera flow visualization. By using this study's results, we can better understand the downwash flow characteristics, which can be used to validate the simulation results with greater accuracy.

As a general overview, this manuscript consists of the following sections: Detailed information about the experimental setup, including the rotor blade and instrumentation, is presented in Section 2, including an analysis of sources of experimental error. Section 3 examines the slipstream boundary and its dynamics, followed by a summary of the findings in Section 4.

2. Materials and methods

2.1. Rotor blade system

Fig. 1 shows the experimental setup used in previous studies [40,41], to measure the velocity fields associated with the rotor blade model of the UAV. Rotor blade test stands were custom fabricated to characterize the vortex trajectory generated from two-bladed rotors at different rotational speeds and vortex ages. A 3 kW electric motor powers the test stand rotor and can produce a rotation speed of 3500 rpm and a thrust of 15.3 kg by the blades. The rotor hub assembly was mounted on the stand three rotor diameters above the ground to verify that no ground effect existed. The rotor blades (Xrotor Pro X8 CW Hobbywing) were composed of two foldable blades. A radius of 370 mm was measured for the whole assembly, including blades, rotor hub, and blade grips, and the rotor solidity was determined to be $\sigma = 0.0327$ for this assembly, as shown in Fig. 2.

2.2. The geometry of the rotor blade

The blade geometry data at different sections is provided in Table 1. The origin of the coordinates is located at the center of the rotor hub, with $\times$ pointing toward the blade tip and z pointing downward, as depicted in Fig. 3, and the rotor radius ($R = 0.37$ m) is used to normalize the coordinate system.

2.3. PIV and the high-speed camera system

2.3.1. Flow visualization using high-speed

The system used for capturing the vortex formation and dynamics in the wake flow in this study consists of a continuous laser (RayPower 5000, Dantec, Denmark), high-speed camera CMOS image sensor (Photron FASTCAM SA-Z 200 K, Japan), seeding generator (9010F0021, Dantec, Denmark), and a control system for managing the speed of the rotor. The high-speed camera captured the blade tip vortex trajectory at early wake ages and captured high frame rates and high temporal resolution images of vortices, allowing the analysis and observation of individual vortices shed from the blade tip in real time as the blades pass through the camera's field of view. The high-speed camera focused on a region of interest with a 1 mega-pixel resolution and was positioned orthogonally to the light sheets, as a result, the field of view was 282 mm $\times$ 282 mm, and the optical resolution was 3.63 pixels /mm. The images were acquired at a frame rate of between 2,000 and 4,000 frames per second.

2.3.2. PIV velocity measurement setup

In addition to the flow visualization using a high-speed camera, and

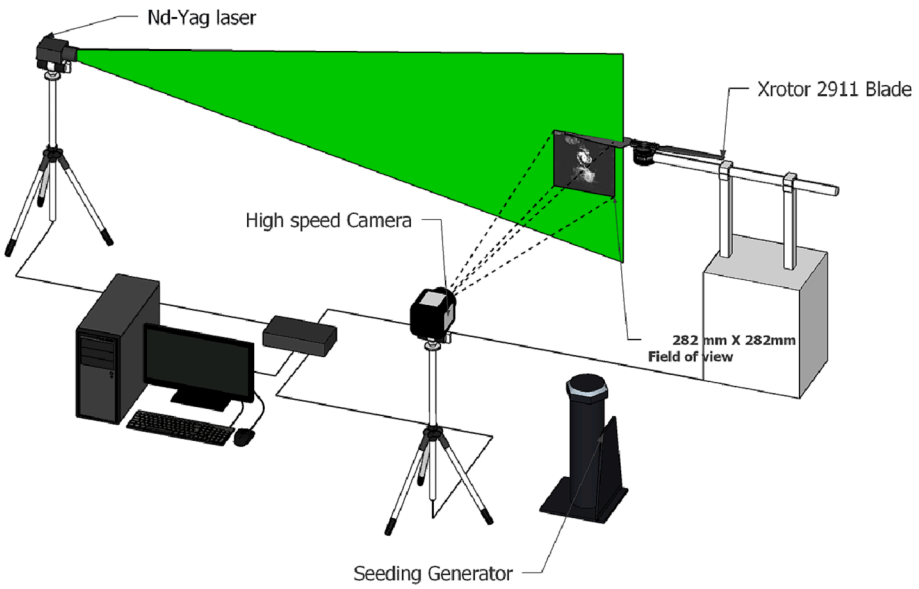

Fig. 1. Schematics of the experimental setup composed of a Nd-YAG laser, high-speed camera, and seeding generator.

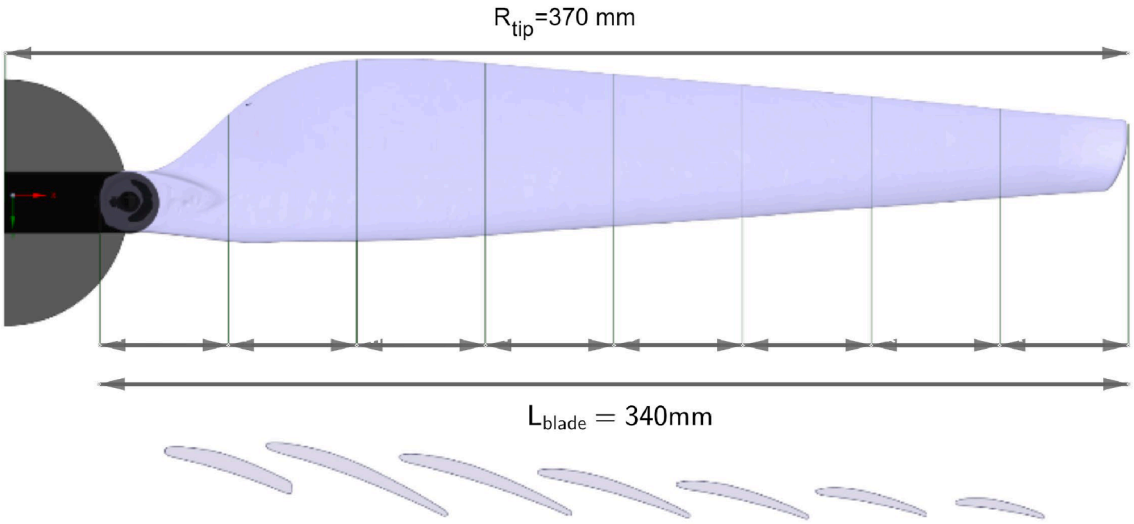

Fig. 2. Three-dimensional model and cross sections of the blade used in the test.

Table 1
Blade Geometry data at different sections.

	1/8 R	2/8 R	3/8 R	4/8 R	5/8 R	6/8 R	7/8 R
Maximum thickness (mm)	5.27	4.84	4.59	4.17	3.77	3.38	3.01
Chord length (mm)	41.22	64.09	60.62	52.83	45.45	37.56	29.85
Maximum camber (mm)	2.18	3.07	2.61	2.56	2.09	1.76	1.59
Pitch angle ∘ (deg)	18.18	21.02	18.45	16.42	14.35	12.09	9.75

to measure and quantify the instantaneous velocity vectors and detailed flow structures such as vortices, a standard two-component velocity PIV measurement system was used, consisting of a double-head Nd-Yag laser (Bigsky laser, QUANTEL, USA) delivering 320 mJ per pulse at 532 nm wavelength and a single double frame CCD camera (2048 by 2048 pixels). The field of view was kept constant and similar to the field of view in the flow visualization part, consequently, the field of view was 282 mm × 282 mm and the optical resolution was 7.26 pixels/mm. The images were captured for a total duration of two seconds for each rpm of the rotor. This was done in free run mode without synchronization with any specific blade. To acquire the PIV images, the rpm of the blades was varied from 1000 to 3000 with 500 rpm increments. This resulted in 34, 50, 67, 84, and 100 revolutions, respectively for the duration of capturing the PIV. An adaptive PIV method with 32x32 pixel interrogation areas with a 50% overlap, which results in 1.09 mm spacing between velocity vectors, is used to analyze the velocity field in order to accurately capture the vortex structure within experimental accuracy.

Based on particle image pairs, velocity vectors were calculated using the adaptive PIV method (DynamicStudio, Dantec, Denmark). After obtaining the velocity vector field, postprocessing concerning the vortex detection and analysis of vortex behavior was carried out in MATLAB using a built-in house code for vortex detection using Γ_2 function. Summary of the procedure of the current study data acquisition and analysis is given in Fig. 4.

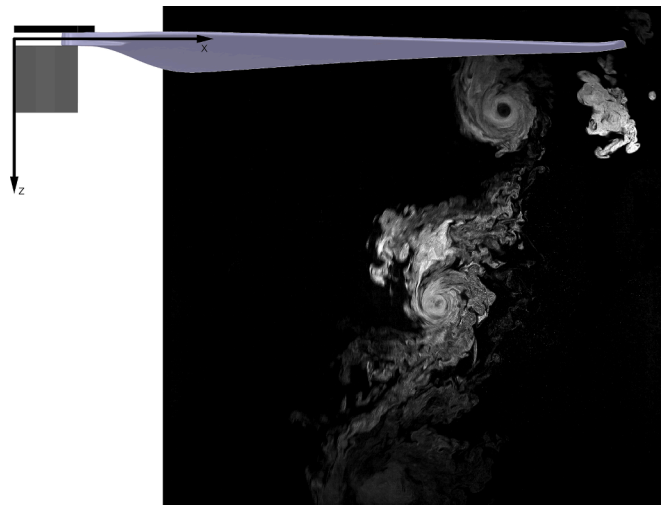

Fig. 3. Schematic of the blade in the view field of the high-speed and PIV camera and the location of the origin of the coordinate system.

2.3.3. Accuracy of data analysis

Particle Image Velocimetry (PIV) systems can accurately measure fluid flow velocities. The accuracy of the system depends on various factors, such as the quality of the camera, the laser, and the seeding particles density, as well as the settings used for acquiring and analyzing the images such as interrogation windows size and Δt between laser pulses. In most cases, PIV systems can achieve accuracies of 1% or better, according to the manufacturer. In the present study the rpm of the rotor was checked and verified with the handheld laser tachometer within accuracy of 1%.

3. Results and discussion

3.1. Visualization of the rotor blade tip vortex with wake age

High-speed camera images were used to analyze the trajectory of vortices with high temporal resolution at different wake ages. Fig. 5 shows the generation and development of the blade tip vortex at wake ages of 0°, 36°, 72°, 108°, 144°, and 180° at 1000 rpm. The yellow dotted lines show the trajectory of the tip vortex center. The vortex is visualized as a small region with high rotational speed and a void at the center of the vortex. Despite the continuous formation of the tip vortex during the passage of the blade through the air, it requires a certain duration for the dispersed fog particles to be ejected from the central region by the centrifugal forces within the vortex. As a result, the visualization of the tip vortex initially appears 1.25 ms after the blade has traversed the laser-illuminated plane, leading to a delay in the visualization of the vortex core. The vortex's path wanders along the main slipstream boundary, and as the vortex wake age rises, so does the amount of wander toward the axis of rotation. The tip vortex moves toward the blade rotation axis faster than the vertical movement as the wake age increases up to the wake age of 180°. As the vortex ages, the rotational speed of the tip vortex decreases, and its core size increases. The tip vortex rotates in the CCW direction, and the inner rotational speed is higher than the outer rotational speed.

Fig. 6 shows the movement of the vortex center at different wake angles of 0°, 45°, 90°, 135°, and 180° with respect to the rotational speed of the blade. As the blade passes through the plane, as shown in Fig. 1, the first vortex is generated. Meanwhile, the blade exerts a force on the vortex generated by the opposite blade, causing the second vortex to move downward faster and slower to the blade hub. As the wake age increases, the distance between the first and second tip vortices increases due to the induced flow of the rotating blades. However, due to mixing flow and reduction in velocity gradient, the distance between the second and third vortices remains unchanged. The distance between the second and third vortices decreases as the rotational speed increases. Other than the tip vortex generated due to the pressure difference between the upper and lower sides of the blade, the upper and lower side boundary layers of the blade merge and form a shear layer. These shear layers are initially horizontal, as indicated by previous studies [9,24,28,42–44]. The inner part of the sheet vortex moves downward faster than the outer part, which resides in the slipstream boundary and becomes oblique (S-shape). Simultaneously, these vortex sheets interact with the previous tip vortices as they move downward together and become laminar as they entrain into the vortex core. It is also observed that as the tip vortex moves in the direction of the blade rotational axis, its size is expanded and diffused as the wake age increases.

3.2. Vorticity analysis of the rotor blade tip vortex

Usually, the vortices in the flow fields are identified using invariants of the velocity gradient tensor. This feature could be used to identify the vortex since the vorticity reaches a local maximum in the center. Fig. 7 shows the instantaneous normalized vorticity $\omega_z c/V_{tip}$ [44]. distributions with wake ages of 45°, 90°, and 135° for 1000 rpm. A cutoff value is used in order to clearly show the normalized vorticity contour. The three tip vortices are shown as concentrated circular regions with a positive, counterclockwise rotation. After normalization of the vorticity it is clear that result is independent from the rpm with a little slight difference between the maximum vorticity at the same wake age. This figure shows that the downwash flow has less of an impact on the first vortex but has a considerable impact on the second and third vortices.

3.3. Vortex identification

Large datasets containing velocity fields were collected using the PIV technique, and identification of the vortex patterns was attempted. The most widely used vortex identification method is based on the local analysis of velocity-gradient tensors and their three invariants. These local vortex-detection criteria are often ineffective for PIV data, especially in regions where the blade passes through the investigating window or the downwash flow is highly turbulent, and blade tip vortices are concentrated. To overcome this matter and find the vortex center accurately, in this study, the Γ_2 function proposed by Graftieaux et al. [45] (Eq. (1)), which relies directly on the topology of the velocity field rather than using velocity derivatives, was used. Using Eq. (1), Γ_2 was calculated according to the proposed correlation at each point x_i in the velocity field. As illustrated in Fig. 8, a 2D domain S_i is shown, in which M is the number of points x_j inside the domain where $i \neq j$, $\vec{n}$ is the unit vector normal to the PIV plain, $\vec{u}_{mean}$ is the average velocity within the domain S_i, and $\vec{u}_j$ is the velocity at point x_j. Γ_2 can distinguish the positions of the vortex center only by considering the topology of the velocity field. In addition, gamma is sufficiently robust to handle large datasets containing many thousands of velocity fields. The value of Γ_2 varies between $-1 \leqslant \Gamma_2 \leqslant 1$, and it is usually between 0.9 and 1 near the vortex center. A simple and robust method for identifying vortical structure centers can be obtained using this definition of Γ_2. The ability to find the vortex center is shown in Fig. 9. This method can accurately determine the tip vortex location despite noisy data due to the blade's passage in PIV images.

$$\Gamma_2\left(\vec{x}_i\right) = \frac{1}{M}\sum_{x_j \in S_i} \frac{\left\{\left(\vec{x}_j - \vec{x}_i\right) \times \left(\vec{u}_j - \vec{u}_{\text{mean}}\right)\right\} \cdot \vec{n}\Big|_0^0}{\left|\vec{x}_j - \vec{x}_i\right|\left|\left(\vec{u}_j - \vec{u}_{\text{mean}}\right)\right|} \tag{1}$$

According to Graftieaux et al. [45], in the proposed correlation, if the 2D domain S is very small and the velocity field is incompressible, then the gamma function depends only on the rotation rate, Ω , the antisymmetric part of the velocity gradient and μ, the eigenvalues of the

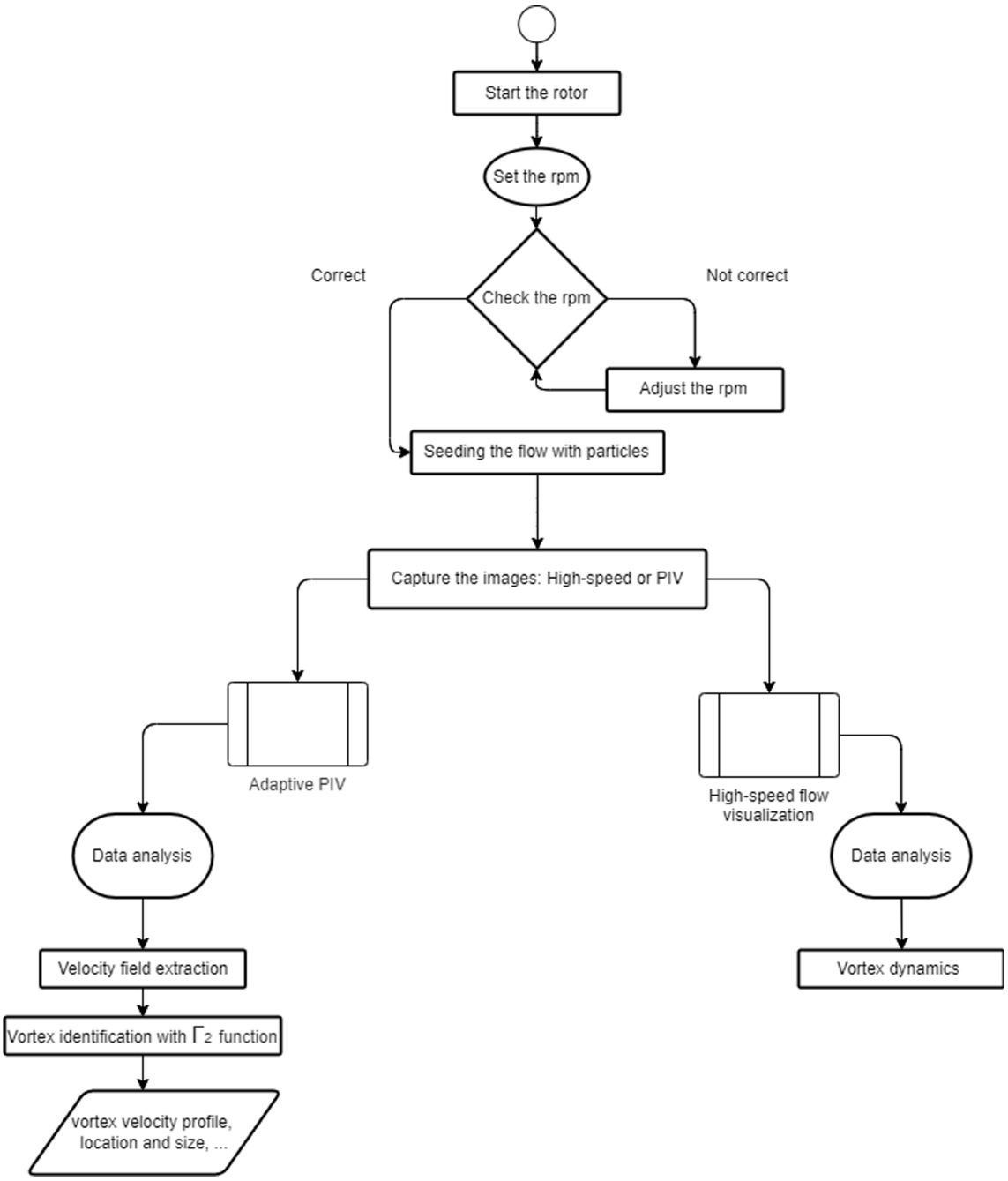

Fig. 4. Flowchart of the current study data acquisition and analysis.

symmetric velocity gradient. In the flow domain when $|\Omega/\mu|\rangle 1$, the flow is dominated mainly by rotation, which corresponds to $|\Gamma_2|\rangle 2/\pi$. The vortex's inner core is defined when $2/\pi \leqslant \Gamma_2 \leqslant 1$, as illustrated by the yellow color in Fig. 9. Using the $\mathbf{\Gamma}_2$ method to find the vortex location, it is clear that the blade tip vortex moves downward and radially in the wake of the rotor. Due to the complex unsteady nature of the rotor's wake, the flow becomes more aperiodic. Fig. 10 shows that the vortex wandering in the lower region of the flow domain is more chaotic for lower rpm.

3.4. Variation in the tip vortex trajectory with the wake age

A comparison of the wake slipstream boundary between the present study and similar previous works [26,31,33,35,39,46] is shown in Fig. 11. The geometrical information and operational status of the rotor blade for the prior and current studies are shown in Table 2. The blades used in these studies have solidity ranging from 0.035 to 0.116, blade radius ranging from 93 mm to 775 mm, and a chord length varying from 18.8 mm to 65 mm. For the present study, the chord length was variable along the blade, and the rotation speed range was between 870 and 3500 rpm. There is a consistent trend in all previous studies and in the current study, which is that at early wake ages, tip vortices are closer to the blade plane and tend to convect more in radial directions than axially, but after passing the following blade, tip vortices tend to move faster axially than they do radially.

In Fig. 12, the center of blade tip vortices is overlaid on the velocity contour of the downwash flow extracted from the time-averaged velocity for 2000 rpm. It can be seen that there is a shear layer region with a velocity deficit between the main downwash flow and the still surrounding air, indicating the typical main slipstream boundary. The

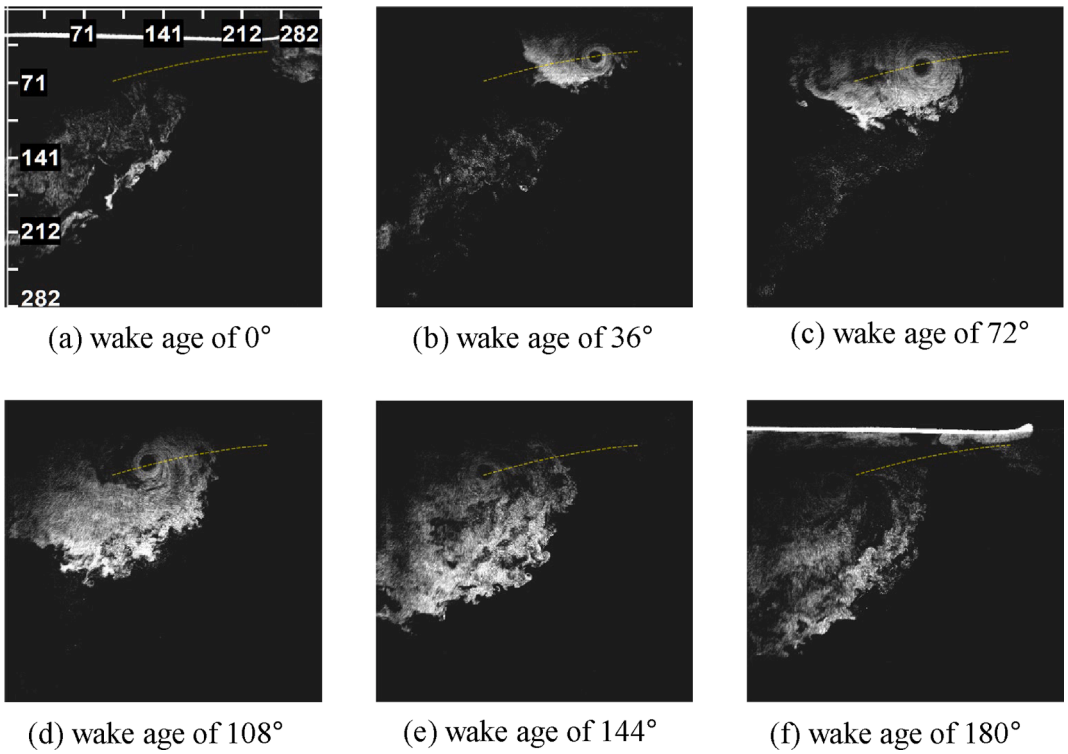

Fig. 5. Visualization of the blade tip vortex at wake ages of 0°, 36°, 72°, 108°, 144°, and 180° at 1,000 rpm. (Image size of 282 mm × 282 mm in X and Y axis).

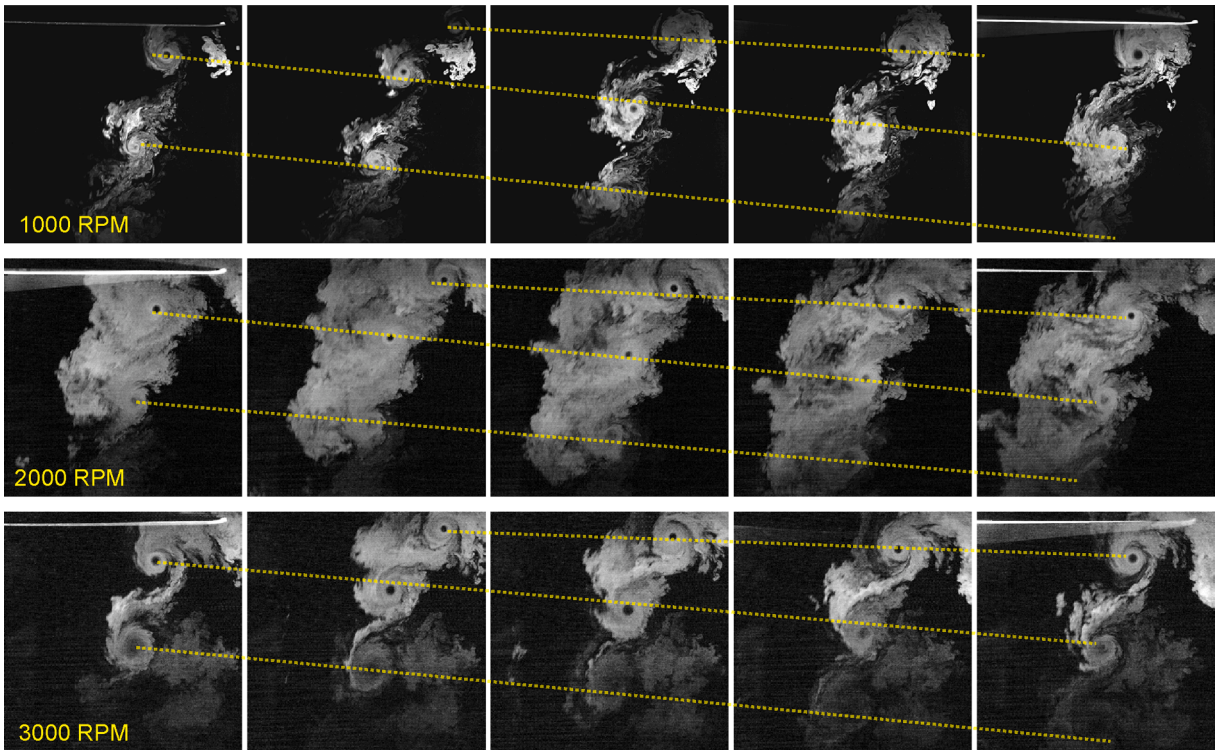

Fig. 6. Development of blade tip vortices at wake ages of 0°, 45°, 90°, 135°, and 180° at 1,000, 2,000, and 3,000 rpm. (image size of 282 mm × 282 mm in X and Y axis).

vortex detection criteria were applied for each of the instantaneous velocity fields. Mostly, blade-tip vortices are contained within the shear layer of the downwash flow along the slipstream boundary. As stated before, due to the roll-up of the horizontal blade's shear layer, the vortices first move in the vicinity of the blade until the vortices reach approximately 180 ($\psi = 360/N_b, N_b = 2$) degrees of the wake. When the opposing blade passes, it exerts a downward force and causes the vortices to change their movement slope and descend at a faster and different rate.

Simple generalized equations can be used to describe wake geome-

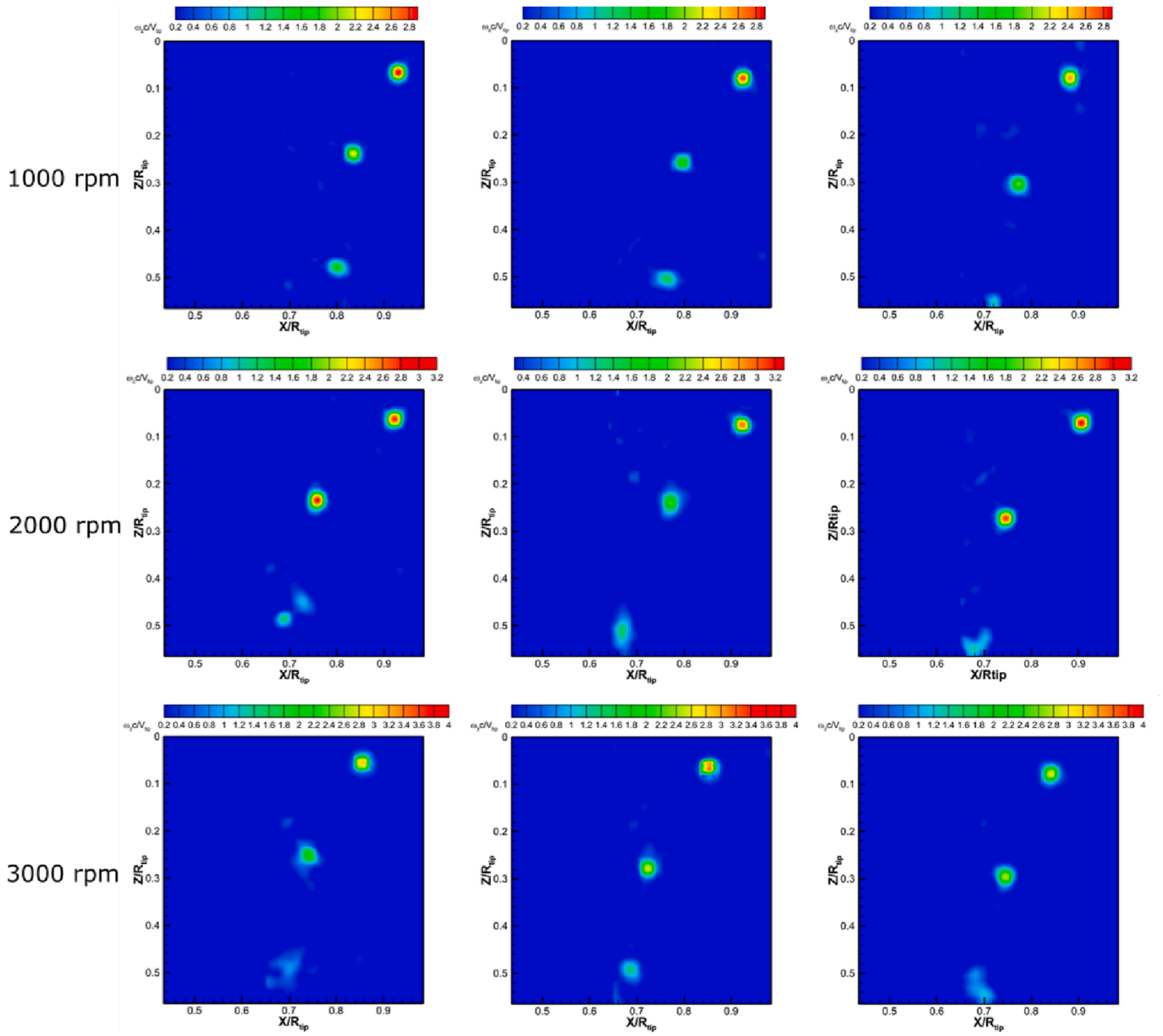

Fig. 7. Instantaneous Vorticity distributions normalized by V_{Btip} with wake ages of 45° to 135° for 1,000, 2,000 and 3,000 rpm.

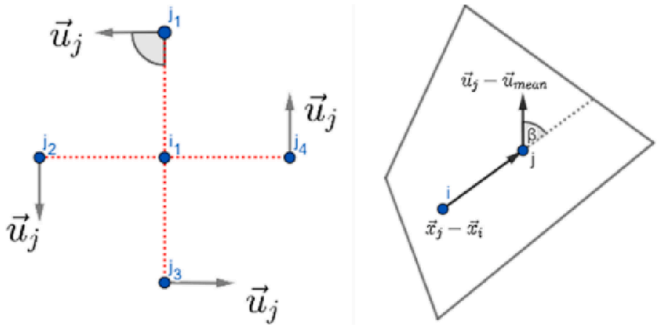

Fig. 8. Domain and components of function used for calculating the vortex location and size.

tries near rotors. This allows rotor wake coordinates to be rapidly determined for various rotor designs and operating conditions. The slipstream boundary was analyzed using wake coordinates in accordance with Landgrebe and Bellinger's analysis [9]. The following relations approximate the axial and radial coordinates for the tip vortex:

$$\frac{Z}{R_{tip}} = \begin{cases} k_1\psi_w & \text{for } 0 \leqslant \psi_w \leqslant 2\pi/N_b \\ \left(\frac{z_{tip}}{R}\right)_{\psi_w = 2\pi/N_b} + k_2\left(\psi_w - \frac{2\pi}{N_b}\right) & \text{for } \psi_w \geqslant 2\pi/N_b \end{cases} \quad (2)$$

$$\frac{X}{R_{tip}} = A + (1-A)\exp(-\Lambda\psi_w) \quad (3)$$

where K_1 and K_2 are as follows:

$$k_1 = -0.25(C_T/\sigma + 0.001\theta_{tw}) \quad (4)$$

$$k_2 = -(1.41 + 0.0141\theta_{tw})\sqrt{C_T/2} \approx -(1 + 0.01\theta_{tw})\sqrt{C_T} \quad (5)$$

For radial coordinates, the coefficients A and Λ are $A = 0.78\Lambda = 0.145 + 27C_T$.

Based on wake visualization data using the high-speed camera, the findings regarding newly generated vortices convection are shown in

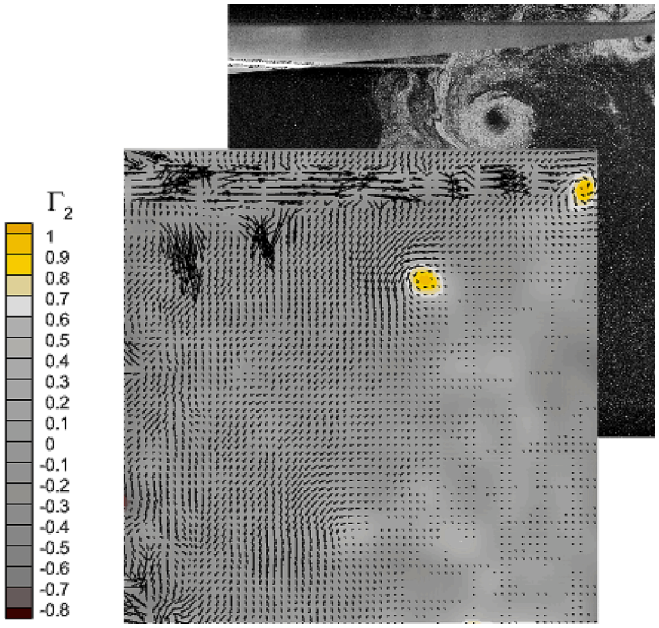

Fig. 9. PIV image with the presence of a blade and the resulting velocity vector field. The yellow and orange spots show the vortex locations determined by the method.

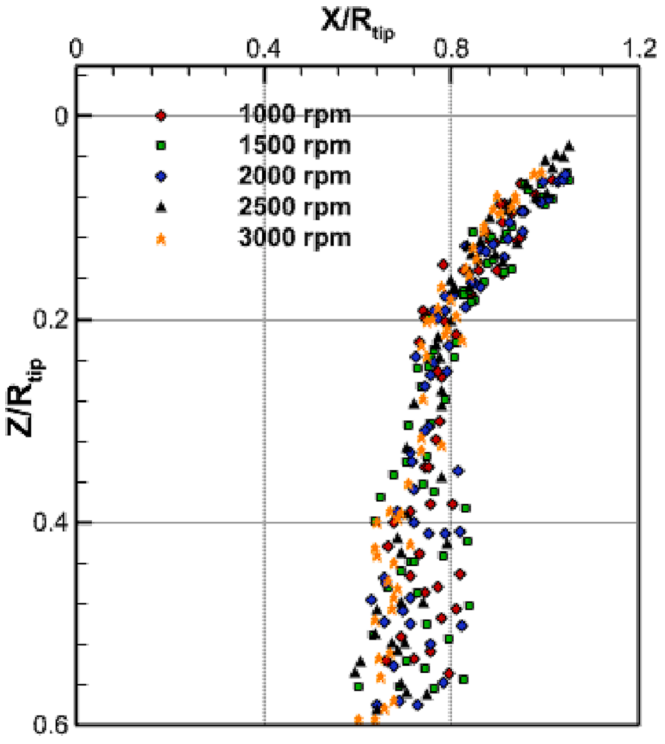

Fig. 10. Tip vortex trajectory in the x- and y-direction for different rotational speeds ranging from 1,000 to 3,000 rpm.

Fig. 13. The tip vortex movements are defined as a function of wake age by these equations. The created vortex moves axially downward at a constant rate determined by the k_1 coefficient until it reaches a wake age of 180°; meanwhile, the radial tip vortex trajectory contracts exponentially. Lines and symbols (circles) in the upper part of the diagram correspond to the vortex axial displacement, while those (triangles) in the lower part correspond to the vortex radial contraction at a given wake age. According to Fig. 13, the deviation from the Landgrebe [9]

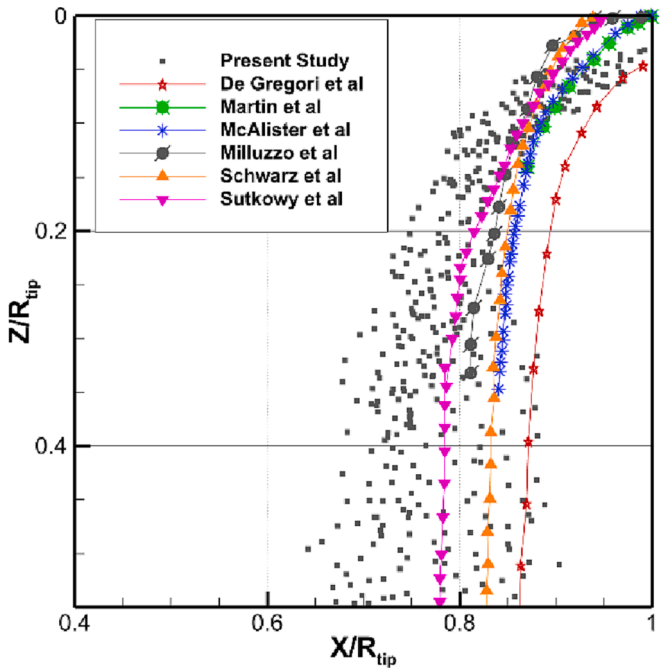

Fig. 11. Wake slip-stream comparison between the current study and previous works.

model equation increases as the rotational speed increases. The axial movement shows more variation than the radial movement. The blades used in the current study were X-rotor 2911, which had variable chord lengths along the blade, whereas all the blades tested by Landgrebe had fixed chord lengths.

For a very long time, measuring the dispersion of tip vortices has been a challenge. Furthermore, the interaction of blade and tip vortices complicates the documentation of such effects. Vortex stretching and intensification can result from close blade-vortex interactions, such as the first blade passage at $\psi = 360/N_b$ degrees.

In describing the structure and evolution of vortices, the vortex core size is a common and significant parameter. An indicator of the intensity of induced effects can be obtained by examining the core size in relation to the maximum swirl velocities. The circle symbols in Fig. 14 illustrate the vortex locations and their sizes in the wake of the rotor. The diameters of the vortices are defined by the distance between the maximum and minimum vortex swirl velocities. There is a relatively rapid growth in the vortex core size. The difficulties in measuring the vortex properties at older wake ages are compounded by the tendency for the flow to become aperiodic.

A comparison of the swirl velocities measured at different wake ages is shown in Fig. 15. The most noticeable feature of the vortices' swirl velocity profile is their lack of symmetry, it is in agreement with the present study result as observed through flow visualization and also the three-dimensional reconstruction of tip vortices conducted by Wolf et al. [36]. These vortices do not possess a circular shape, indicating that the corresponding streamlines are also non-circular due to the downwash velocity and the effect of the force exerted by opposing blade.

In flow visualization experiments, it is not uncommon to observe the particle void in the vortex core. This is the result of centrifugal forces and the higher density of the seeding particles compared to air. According to Ramasamy et al. [47] the peak swirl velocity is found outside of the void, and the Particle Image Velocimetry (PIV) adaptive algorithm fill the void within the vortex core. Accidentally the value inside vortex core interpolated by PIV method is similar to the laminar profile velocity of the vortex but due to lack of seeding particle and interpolating based on the neighboring interrogation windows, the values of the velocity inside the vortex core is less reliable. The peak values of the swirl

Table 2
Summary of the blade geometry and operating conditions.

	[17]	(Kenneth W. McAlister, 2004)	[22]	[40]	[3]	[35]	**Present Study**
Radius (mm)	406	957.6	408	93.5	360	775	370
Chord (mm)	44.5	103.9	44.5	18.8	32.7	61	Variable
Tip Speed (m/s)	89.3	87.2	89.7	34.3	67.1	101.8	38.72 ~ 116.18
Blade linear twist	Untwisted	7.55	17	Untwisted	Untwisted	untwisted	8
Solidity	0.035	0.069	0.0697	0.058	0.116	0.05	0.065
Rotational speed (rpm)	1800	870	2100	3500	1780	1254	1000 ~ 3000

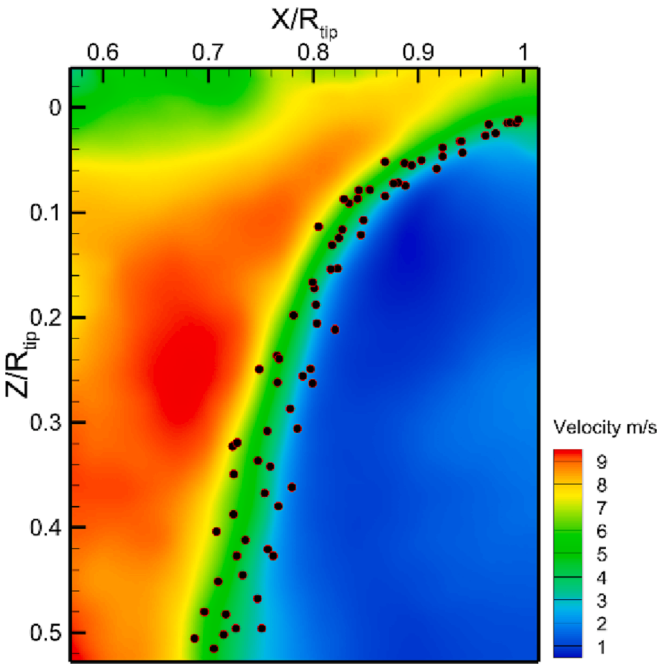

Fig. 12. Velocity contours of downwash flow overlaid by vortex location at different wake ages for 2000 rpm.

velocity show a decreasing trend as the wake ages. Before a wake age of 180°, the maximum swirl velocity of vortices shows a logarithmic decreasing trend; meanwhile, the minimum value of swirl velocity shows the opposite trend. In Fig. 16, after passing the opposite blade at the wake age of 180°, the maximum swirl velocity shows a noticeable change in the trend. As the wake ages, the velocity peaks on either side of the vortex core decrease and move toward becoming more symmetrical.

To develop and validate vortex models, it is helpful to examine vortices at various wake ages and rotor operating conditions to determine whether the vortex flow follows a self-similar pattern. The swirl velocity was normalized with respect to the core radius and peak swirl velocity. Based on the measurements for 2,000 rpm, as shown in Fig. 17a, and Fig. 17b, there is approximately a self-similarity between the various vortex and their circulation at different ages. While the vortices outside of the vortex core are in the transition zone, the self-similar velocity profile inside the vortex core resembles the Iverson model's laminar profile, and it is in good agreement with the flow visualization images in Fig. 17c that there is laminar flow within the vortex's core. The self-similar velocity profile shows that outside of the vortex core, the structure is neither entirely laminar nor entirely turbulent, as shown in the vortex visualization images in Fig. 17c. The best model that fits the measured data outside of the vortex core is the Vatistas [48] vortex model (Eq. (6)) with $\beta = 1.38$ and $n = 2$, solid line in Fig. 17a, and Fig. 17b.

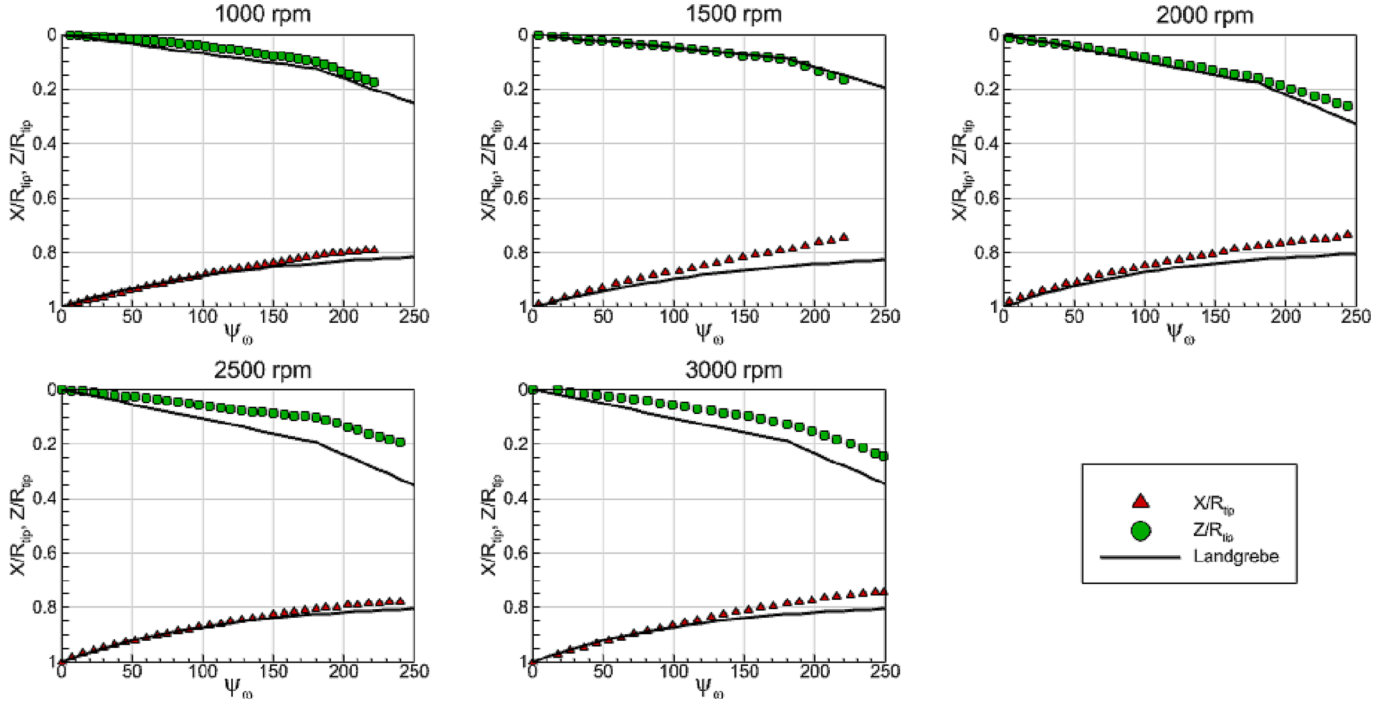

Fig. 13. Wake axial () and radial () coordinates for rotational speeds from 1000 rpm to 3000 rpm.

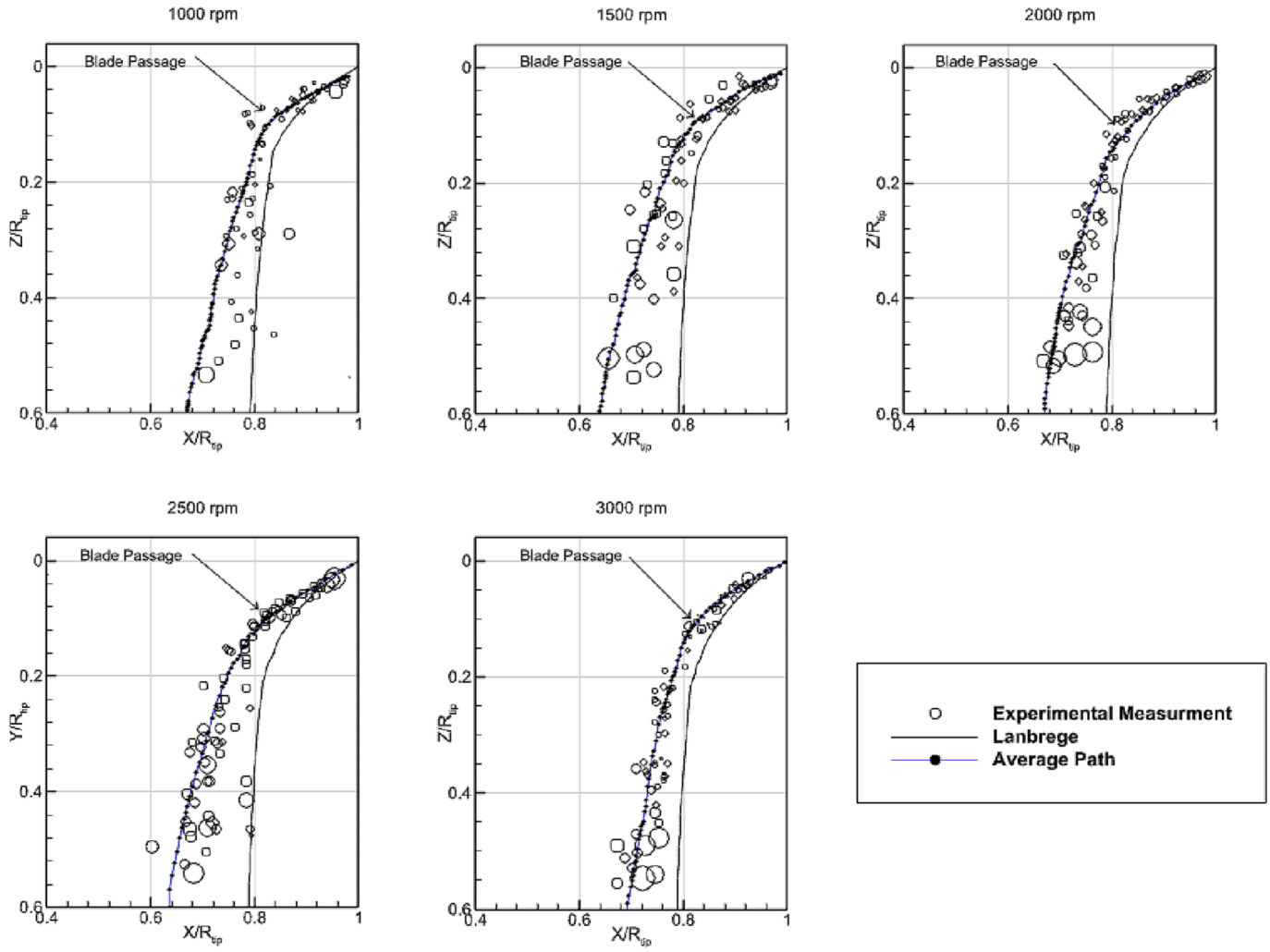

Fig. 14. Position of the tip vortices and their size at different rotational speeds, where the symbols indicate the size of the vortices.

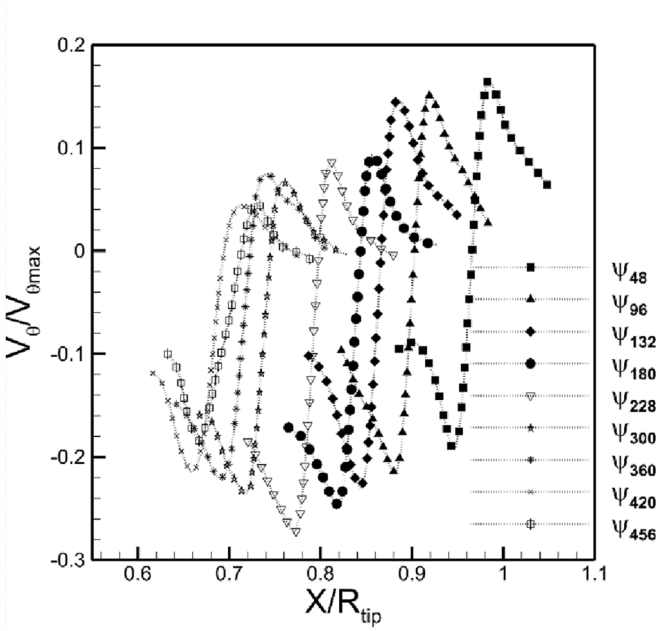

Fig. 15. Swirl velocity profile with respect to the nondimensional radial position at different wake ages for 2,000 rpm.

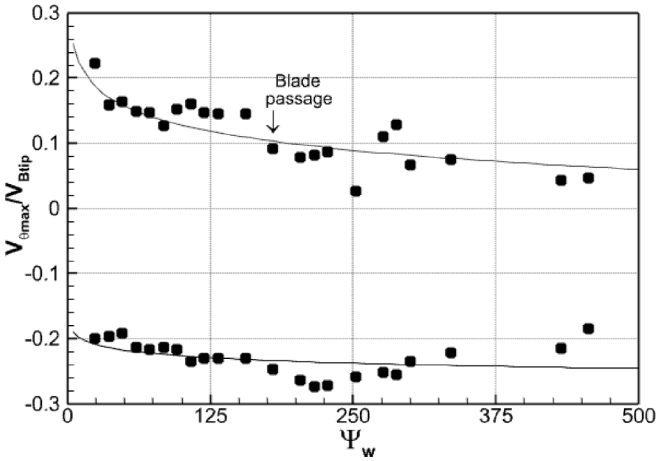

Fig. 16. Peak swirl velocity of vortices at different wake ages.

$$\frac{V_\theta}{V_{\theta,\max}} = \frac{r}{r_c}\left(\frac{1+\beta}{1+\beta(r/r_c)^{2n}}\right)^{\frac{1+\beta}{2n\beta}} \tag{6}$$

A normalized circulation profile based on the core circulation $2\pi V_{\theta_{\max}} r_c$ is shown in Fig. 17b. Likewise, all circulation distributions around the vortex core at different wake ages showed self-similar

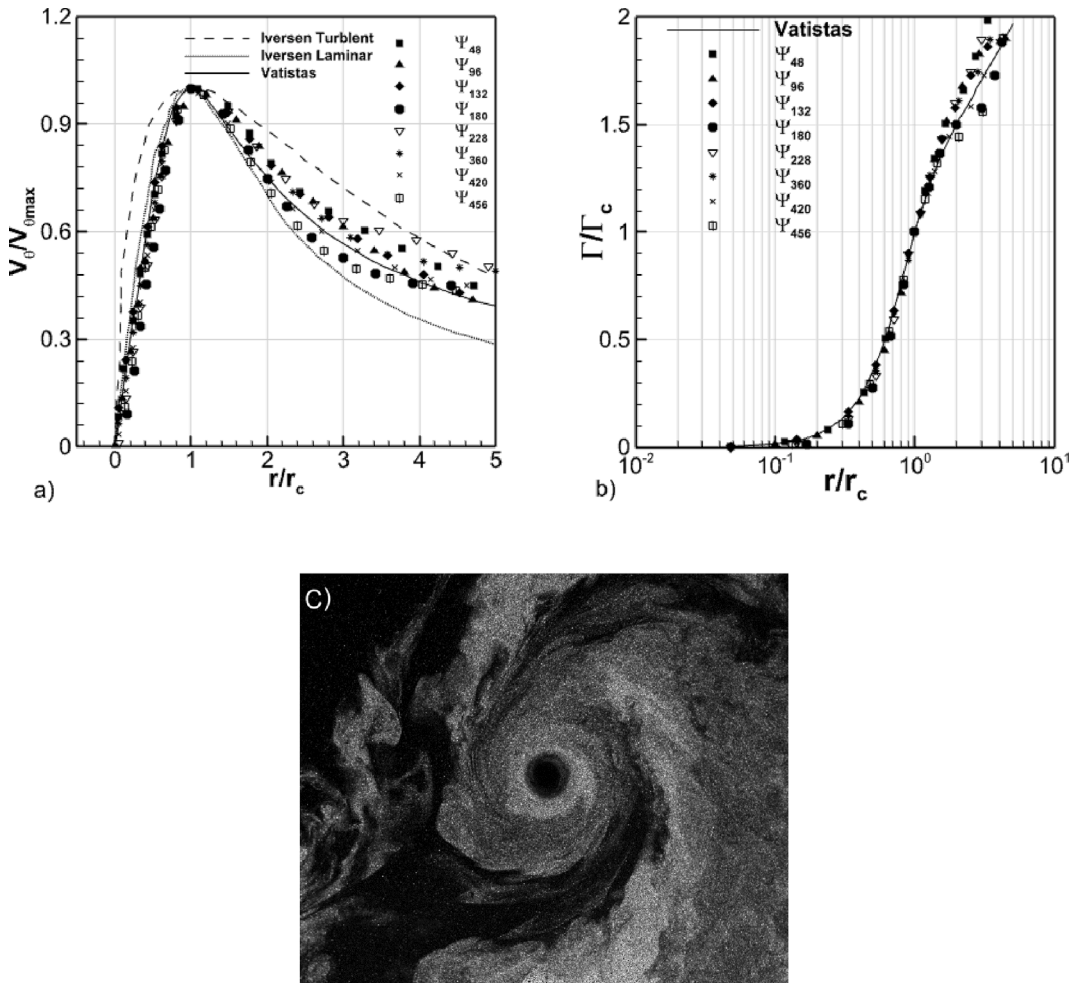

Fig. 17. A) vortex swirl velocity profiles, b) self-similar nondimensional vortex circulation in comparison with the Iversen and Vatistas models, and c) vortex visualization at.

behavior as the vortex grew older, merging into a single curve.

4. Conclusion

The qualitative and statistical characteristics of typical agricultural unmanned aerial vehicle blade tip vortices and rotor wakes were studied to gain an understanding of vortex-downwash interactions. A two-dimensional particle image velocimetry system combined with a high-speed camera was used at various rotational speeds to capture the velocity field of downwash flow, trajectory of the tip vortex, swirl velocity, and vorticity intensity of the tip vortex at different wake ages. The following summarizes the key conclusions of the current work:

Because of the pressure difference between the upper and lower sides of the blade, a tip vortex forms as the blade passes through the plane, causing the vortex to roll into the downwash flow. When the opposing blade exerts forces on the tip vortex generated by the previous blade, which now has the wake age $\psi = 180$, the vortex moves downward at a different rate. The velocity field acquired from particle image velocimetry measurement was subjected to the Γ_2 vortex identification criteria. In older wake ages, the vortex flow takes on an aperiodic pattern, making it more challenging to measure vortex features. The primary downwash and the still surrounding air were separated by a shear layer zone that has a velocity deficit. Blade-tip vortices are contained within the shear layer, wandering along the slipstream boundary. For rotor wake geometries near the rotor blade, simple generalized equations can be used to quickly determine rotor wake coordinates for different designs and operating conditions. A discrepancy between the experimental data and Landgrebe's model was observed due to the difference in blade geometry between the described model and the current study. The effect of blade geometry is substantial, and we have not yet fully explored in this study. However, the overall trend remains the same, while further study is needed to develop a model that accounts for other blade characteristics. A blade's geometry clearly affects a system's performance, and thus a better understanding of how this affects performance is essential.

When the tip vortices generated by rotors have a non-axisymmetric structure because probably due the downwash effect of the opposing blade. As the vortices age, the velocity of the swirl peak decreases logarithmically. Despite this, the swirl velocity structure of the tip vortices shows a self-similar structure that can be used to validate vortex models. The nondimensional swirl velocity of vortices within the vortex core exhibits a comparable self-similar velocity profile to the laminar profile of the Iverson model despite the transition zone outside of the vortex core. The distributions of circulation around the vortex core at different wake ages also showed self-similar behavior as the vortex grew older, eventually merging into one.

CRediT authorship contribution statement

Mehrzad Ansaripour: Software, Validation, Formal analysis, Writing – original draft, Visualization, Investigation. **Reza Alidoost Dafsari:** Validation, Formal analysis, Writing – original draft, Visualization, Investigation. **Seung-Hwa Yu:** Conceptualization. **Yong Choi:** Conceptualization. **Jeekeun Lee:** Conceptualization, Supervision,

Writing – review & editing.

Declaration of Competing Interest

The authors declare that they have no known competing financial interests or personal relationships that could have appeared to influence the work reported in this paper.

Data availability

Data will be made available on request.

Acknowledgment

This research was supported by the "Cooperative Research Program for Agriculture Science and Technology Development", Project number PJ017065022022 Rural Development Administration, Republic of Korea.

References

[1] C. Ju, H. Son, Multiple UAV systems for agricultural applications: control, Implementation, and Evaluation, Electronics 7 (2018) 162, https://doi.org/10.3390/electronics7090162.
[2] P. Radoglou-Grammatikis, P. Sarigiannidis, T. Lagkas, I. Moscholios, A compilation of UAV applications for precision agriculture, Comput. Netw. 172 (2020), 107148, https://doi.org/10.1016/j.comnet.2020.107148.
[3] T. Talaviya, D. Shah, N. Patel, H. Yagnik, M. Shah, Implementation of artificial intelligence in agriculture for optimisation of irrigation and application of pesticides and herbicides, Artif. Intell. Agric. 4 (2020) 58–73, https://doi.org/10.1016/j.aiia.2020.04.002.
[4] L. Kováčik, A. Novák, Comparison of Aerial Application vs, Ground Application, Transp. Res. Procedia. 44 (2020) 264–270, https://doi.org/10.1016/j.trpro.2020.02.044.
[5] P.A. Morales-Rodríguez, E. Cano Cano, J. Villena, J.A. López-Perales, A comparison between conventional sprayers and new UAV Sprayers: a study case of vineyards and olives in extremadura (Spain), Agronomy 12 (2022) 1307, https://doi.org/10.3390/agronomy12061307.
[6] L. Li, Y. Liu, X. He, J. Song, A. Zeng, W. Zhichong, L. Tian, Assessment of spray deposition and losses in the apple orchard from agricultural unmanned aerial vehicle in China, in: 2018 Detroit Mich. July 29 - August 1 2018, American Society of Agricultural and Biological Engineers, 2018. https://doi.org/10.13031/aim.201800504.
[7] W.-C. Qin, B.-J. Qiu, X.-Y. Xue, C. Chen, Z.-F. Xu, Q.-Q. Zhou, Droplet deposition and control effect of insecticides sprayed with an unmanned aerial vehicle against plant hoppers, Crop Prot. 85 (2016) 79–88, https://doi.org/10.1016/j.cropro.2016.03.018.
[8] T. Qing, Z. Ruirui, C. Liping, X. Min, Y. Tongchuan, Z. Bin, Droplets movement and deposition of an eight-rotor agricultural UAV in downwash flow field, Int. J. Agric. Biol. Eng. 10 (2017) 47–56, https://doi.org/10.25165/ijabe.v10i3.3075.
[9] A.J. Landgrebe, The wake geometry of a hovering helicopter rotor and its influence on rotor performance, J. Am. HelicopterSoc. 17 (1972) 3–15, https://doi.org/10.4050/JAHS.17.4.3.
[10] C. Tung, S.L. Pucci, F.X. Caradonna, H.A. Morse, The structure of trailing vortices generated by model rotor blades. Eur. Rotorcr. Powered Lift Aircr., Forum, Germany, 1981.
[11] N. Bloise, M. Carreno Ruiz, D. D'Ambrosio, G. Guglieri, Wind Tunnel Testing of Remotely Piloted Aircraft Systems for Precision Crop-Spraying Applications, in: 2021 IEEE Int. Workshop Metrol. Agric. For. MetroAgriFor, IEEE, Trento-Bolzano, Italy, 2021, pp. 378–383. https://doi.org/10.1109/MetroAgriFor52389.2021.9628600.
[12] S. Grant, J. Perine, F. Abi-Akar, T. Lane, B. Kent, C. Mohler, C. Scott, A. Ritter, A wind-tunnel assessment of parameters that may impact spray drift during UAV pesticide application, Drones. 6 (2022) 204, https://doi.org/10.3390/drones6080204.
[13] T. Qing, Z. Ruirui, C. Liping, X. Min, Y. Tongchuan, Z. Bin, Droplets movement and deposition of an eight-rotor agricultural UAV in downwash flow field, Biol. Eng. 10 (n.d.).
[14] K.W. McAlister, Rotor wake development during the first revolution, J. Am. Helicopter Soc. 49 (2004) 371–390.
[15] W. Ling, C. Du, Y. Ze, N. xindong, W. Shumao, Research on the prediction model and its influencing factors of droplet deposition area in the wind tunnel environment based on UAV spraying, IFAC-Pap. 51 (2018) 274–279, https://doi.org/10.1016/j.ifacol.2018.08.174.
[16] P.B. Martin, G.J. Pugliese, J.G. Leishman, High resolution trailing vortex measurements in the wake of a hovering rotor, J. Am. Helicopter Soc. 48 (2003) 39–52, https://doi.org/10.4050/JAHS.48.39.
[17] M. Ramasamy, J.G. Leishman, A reynolds number-based blade tip vortex model, J. Am. Helicopter Soc. 52 (2007) 214–223, https://doi.org/10.4050/JAHS.52.214.
[18] M. Ramasamy, J.G. Leishman, A generalized model for transitional blade tip vortices, J. Am. Helicopter Soc. 51 (2006) 92, https://doi.org/10.4050/1.3092881.
[19] R. Jain, Sensitivity study of high-fidelity hover predictions on the sikorsky S-76 Rotor, J. Aircr. 55 (2018) 78–88, https://doi.org/10.2514/1.C034076.
[20] S. Uluocak, M. Perçin, O. Uzol, Experimental investigation of tip anhedral effects on the aerodynamics of a model helicopter rotor in hover, Aerosp. Sci. Technol. 113 (2021), 106671, https://doi.org/10.1016/j.ast.2021.106671.
[21] J. Milluzzo, A. Sydney, J. Rauleder, J.G. Leishman, In-ground-effect aerodynamics of rotors with different blade tips, Annu. Forum Proc. - AHS Int. 1 (2010) 697–720.
[22] H. Zhang, L. Qi, J. Wan, E.M. Musiu, J. Zhou, Z. Lu, P. Wang, Numerical simulation of downwash airflow distribution inside tree canopies of an apple orchard from a multirotor unmanned aerial vehicle (UAV) sprayer, Comput. Electron. Agric. 195 (2022), 106817, https://doi.org/10.1016/j.compag.2022.106817.
[23] B. Esakki, P. Gokul Raj, L.-J. Yang, E. Khurana, S. Khute, P. Vikram, Computational Fluid Dynamic Analysis of Amphibious Unmanned Aerial Vehicle, J. Appl Comput. Mech. (2020), https://doi.org/10.22055/jacm.2020.32461.2018.
[24] Q. Shi, Y. Pan, B. He, H. Zhu, D. Liu, B. Shen, H. Mao, The airflow field characteristics of UAV Flight in a greenhouse, Agriculture. 11 (2021) 634, https://doi.org/10.3390/agriculture11070634.
[25] L. Wang, M. Xu, Q. Hou, Z. Wang, Y. Lan, S. Wang, Numerical verification on influence of multi-feature parameters to the downwash airflow field and operation effect of a six-rotor agricultural UAV in flight, Comput. Electron. Agric. 190 (2021), 106425, https://doi.org/10.1016/j.compag.2021.106425.
[26] K. McAlister, J. Heineck, Measurements of the Early Development of Trailing Vorticity from a Rotor, (2002).
[27] M. Ramasamy, B. Johnson, T. Huismann, J.G. Leishman, An Improved Method for Estimating Turbulent Vortex Flow Properties From Stereoscopic DPIV Measurements, in: Annu. FORUM Proc.-Am. HELICOPTER Soc., AMERICAN HELICOPTER SOCIETY, INC, 2007: p. 1974.
[28] M. Ramasamy, T.E. Lee, J.G. Leishman, Flowfield of a rotating-wing micro air vehicle, J. Aircr. 44 (2007) 1236–1244, https://doi.org/10.2514/1.26415.
[29] K. Duraisamy, M. Ramasamy, J.D. Baeder, J.G. Leishman, High-resolution computational and experimental study of rotary-wing tip vortex formation, AIAA J. 45 (2007) 2593–2602, https://doi.org/10.2514/1.26575.
[30] B. Johnson, M. Ramasamy, J.G. Leishman, Turbulence measurements inside blade tip vortices using dual-plane particle image velocimetry, J. Am. Helicopter Soc. 55 (2010), 042007, https://doi.org/10.4050/JAHS.55.042007.
[31] J. Milluzzo, J.G. Leishman, Fluid dynamics of the helicoidal wake sheets trailed from a hovering rotor, J. Am. Helicopter Soc. 61 (2016) 1–17, https://doi.org/10.4050/JAHS.61.012002.
[32] D. Shukla, N. Komerath, Multirotor drone aerodynamic interaction investigation, Drones. 2 (2018) 43, https://doi.org/10.3390/drones2040043.
[33] M.L. Sutkowy, A. Pandey, M. McCrink, J.W. Gregory, Rotor Wake Structure Development in Low Reynolds Number Conditions, in: 2018 AIAA Aerosp. Sci. Meet., American Institute of Aeronautics and Astronautics, Kissimmee, Florida, 2018. 10.2514/6.2018-1830.
[34] H. Du, W. Kong, Y. Wang, W. Liu, M. Huang, W. Zhang, M. Tang, Research on rotorcraft blade tip vortex identification and motion characteristics in hovering state, Symmetry 12 (2020) 196, https://doi.org/10.3390/sym12020196.
[35] F. De Gregorio, A. Visingardi, G. Iuso, An experimental-numerical investigation of the wake structure of a hovering rotor by PIV combined with a Γ2 vortex detection criterion, Energies 14 (2021) 2613, https://doi.org/10.3390/en14092613.
[36] C.C. Wolf, C. Schwarz, K. Kaufmann, A.D. Gardner, D. Michaelis, J. Bosbach, D. Schanz, A. Schröder, Experimental study of secondary vortex structures in a rotor wake, Exp. Fluids 60 (2019) 175, https://doi.org/10.1007/s00348-019-2807-1.
[37] N.M. Chaderjian, Advances in rotor performance and turbulent wake simulation using DES and adaptive mesh refinement, in, Seventh Int. Conf. Comput. Fluid Dyn. ICCFD7 (2012).
[38] N.S. Hariharan, T.A. Egolf, L.N. Sankar, Simulation of Rotor in Hover: Current State, Challenges and Standardized Evaluation, in: 52nd Aerosp. Sci. Meet., American Institute of Aeronautics and Astronautics, National Harbor, Maryland, 2014. 10.2514/6.2014-0041.
[39] C. Schwarz, A. Bodling, C.C. Wolf, R. Brinkema, M. Potsdam, A.D. Gardner, Development of secondary vortex structures in rotor wakes, Exp. Fluids 63 (2022) 4, https://doi.org/10.1007/s00348-021-03348-8.
[40] C. Shouji, S.-H. Yu, Y.-H. Kang, Y. Choi, R.A. Dafsari, J. Lee, Experimental analysis of the downwash airflow created by a single rotor blade in agricultural drones, J. Biosyst. Eng. 46 (2021) 317–331, https://doi.org/10.1007/s42853-021-00109-7.
[41] C. Shouji, R. Alidoost Dafsari, S.-H. Yu, Y. Choi, J. Lee, Mean and turbulent flow characteristics of downwash air flow generated by a single rotor blade in agricultural drones, Comput. Electron. Agric. 190 (2021), 106471, https://doi.org/10.1016/j.compag.2021.106471.
[42] M. Ramasamy, B. Johnson, J.G. Leishman, Turbulent tip vortex measurements using dual-plane stereoscopic particle image velocimetry, AIAA J. 47 (2009) 1826–1840, https://doi.org/10.2514/1.39202.
[43] M. Ramasamy, B. Johnson, J.G. Leishman, Understanding the aerodynamic efficiency of a hovering micro-rotor, J. Am. Helicopter Soc. 53 (2008) 412, https://doi.org/10.4050/JAHS.53.412.
[44] C.C. Wolf, J.N. Braukmann, W. Stauber, T. Schwermer, M. Raffel, The tip vortex system of a four-bladed rotor in dynamic stall conditions, J. Am. Helicopter Soc. 64 (2019) 1–14, https://doi.org/10.4050/JAHS.64.022005.
[45] L. Graftieaux, M. Michard, N. Grosjean, Combining PIV, POD and vortex identification algorithms for the study of unsteady turbulent swirling flows, Meas.

Sci. Technol. 12 (2001) 1422–1429, https://doi.org/10.1088/0957-0233/12/9/307.
[46] P. Martin, J. Leishman, Trailing Vortex Measurements in the Wake of a Hovering Rotor Blade with Various Tip Shapes, (2003).
[47] M. Ramasamy, R. Paetzel, M.J. Bhagwat, Aperiodicity correction for rotor tip vortex measurements, in: 2011, pp. 2903–2916.
[48] G.H. Vatistas, G.D. Panagiotakakos, F.I. Manikis, Extension of the n-vortex model to approximate the effects of turbulence, J. Aircr. 52 (2015) 1721–1725, https://doi.org/10.2514/1.C033238.